J. Geomag. Geoelectr., 46, 669–692, 1994

The Low Energy Particle (LEP) Experiment onboard the GEOTAIL Satellite

T. MUKAI[1], S. MACHIDA[2], Y. SAITO[1], M. HIRAHARA[3], T. TERASAWA[3], N. KAYA[4], T. OBARA[1], M. EJIRI[5], and A. NISHIDA[1]

[1]*The Institute of Space and Astronautical Science, Kanagawa 229, Japan*
[2]*Geophysical Institute, Kyoto University, Kyoto 606, Japan*
[3]*Department of Earth and Planetary Physics, University of Tokyo, Tokyo 113, Japan*
[4]*Faculty of Engineering, Kobe University, Kobe 657, Japan*
[5]*National Institute of Polar Research, Tokyo 173, Japan*

(Received November 1, 1993; Revised January 31, 1994; Accepted February 9, 1994)

The low energy particle (LEP) instrument onboard GEOTAIL is designed to make comprehensive observations of plasma and energetic electrons and ions with fine temporal resolution in the terrestrial magnetosphere (mainly magnetotail) and in the interplanetary medium. It consists of three units of sensors (LEP-EA, LEP-SW and LEP-MS) and a common electronics (LEP-E). The Energy-per-charge Analyzers (EA) measure three-dimensional velocity distributions of electrons (with EA-e) and ions (with EA-i), simultaneously and separately, over the energy-per-charge range of several eV/q to 43 keV/q. Emphasis in the EA design is laid on the large geometrical factor to measure tenuous plasma in the magnetotail with sufficient counting statistics in the high-time-resolution measurement. On the other hand, the Solar Wind ion analyzer (SW) has smaller geometrical factor, but fine angular and energy resolutions, to measure energy-per-charge spectra of the solar wind ions. In both EA and SW sensors, the complete three-dimensional velocity distributions can only be obtained in a period of four spins, while the velocity moments up to the third order are calculated onboard every spin period (nominally, 3 sec). The energetic-ion Mass Spectrometer (MS) can provide three-dimensional determinations of the ion composition. In this paper, we describe the instrumentation and present some examples of the inflight measurements.

1. Introduction

Because of the interaction with the solar wind, the Earth's dipole-like magnetic field is deformed into a shape that is compressed on the dayside and stretched out into a geomagnetic tail on the nightside. The presence of the geomagnetic tail and the associated cross-tail current represents excess energy imparted from the solar wind through the magnetopause and stored in the magnetosphere. The principal purpose of GEOTAIL is to clarify mechanisms of input, storage, release and conversion of energy in the magnetotail. The GEOTAIL mission is expected to play an important role in the International Solar Terrestrial Physics (ISTP)-Global Geospace Science (GGS) program to study energy, momentum and mass flow in this geospace environment. The GEOTAIL satellite was successfully launched on July 24, 1992, into a translunar orbit optimized to swingby the moon at ~1500 UT on September 8, 1992, after 4.5 revolutions around the earth. Then, after the first lunar swingby as planned, the spacecraft was injected into a double-lunar-swingby geotail orbit with apogee of distances of 220 Re on the nightside. In Fall 1994, the spacecraft will be maneuvered to a low-inclination orbit with perigee of 8 Re and apogee of 30 Re. Some important issues on the magnetotail physics are addressed below.

The magnetotail has been thought to consist of various plasma regimes, such as the plasma mantle, low-latitude boundary layers, tail lobes and plasma sheet regions. One paradigm for the magnetotail dynamics is a reconnection-convection model. In this model, the mantle field lines undergo convection toward the plasma sheet and become reconnected in the distant tail. At the plasma-sheet boundary layer, there are high-speed ion beams streaming earthward, which become counterstreaming because of

mirroring in the strong-field region near the Earth and eventually evolve into the hot, nearly isotropic plasma sheet (e.g., Eastman *et al.*, 1984; Takahashi and Hones, 1988; Nakamura *et al.*, 1992). Plasmas and magnetic field lines convect earthward in the plasma sheet. During the last decade, considerable progress has been made in understanding of the magnetotail plasma by ISEE-1/2 and AMPTE observations in the near-earth region of the magnetotail (e.g., Lui, 1987; Baumjohann, 1993 and references therein), while ISEE-3 observations enhanced our understanding of the distant tail (e.g., ISEE-3 Distant Geotail Results, 1984). While these observations have been shown to be compatible with the general features of the above model, there have remained a number of points which have not yet been clarified by observations. Examples are the source of plasma, the validity of the reconnection-convection model as described above under the condition of the northward interplanetary magnetic field, and the structure and temporal development of the plasmoid.

It is now well known that both solar wind and ionospheric plasmas contribute to the plasma sheet, and these sources vary according to the global magnetospheric activity (Peterson *et al.*, 1981; Lennartsson *et al.*, 1981; Sharp *et al.*, 1982). The plasma temperature in the plasma sheet is much higher than those of the solar wind and the ionospheric plasma. One open question is how the plasma is transported to the plasma sheet from the source regions, and how and where the plasmas are energized. Ashour-Abdalla *et al.* (1993) have shown some results of the test particle simulations, in which particles in the plasma mantle are convected into the plasma sheet and energized in the current sheet through the Speiser orbit (e.g., Speiser, 1965; Lyons and Speiser, 1982). Delcourt *et al.* (1993) have demonstrated, by means of three-dimensional particle codes, that the low-energy ionospheric protons can significantly contribute to the populations of the plasma sheet and the centrifugal force around the plasma sheet boundary layer is important for energization of the low-energy particles. However, particle entry and energization processes have not yet been identified observationally. Another potential source might be the low-latitude boundary layer (LLBL), but the generation mechanism of the LLBL has not been identified either theoretically or observationally.

Release of the stored energy takes place often explosively as a substorm, in which the magnetic energy is converted into plasma kinetic energy in a certain region of the magnetotail. In the inner magnetosphere, the energized particles precipitate into the polar upper-atmosphere, resulting in auroral breakup, and are injected into the radiation belt, while on the tailward side plasmoids flow tailward with speeds of several hundreds km/s in the distant tail (e.g., Hones *et al.*, 1984; Baker *et al.*, 1987). Various substorm models (e.g., Lui, 1991), such as the near-earth reconnection model, the current-wedge model, and the magnetosphere-ionosphere coupling model, have been proposed. However, we do not know exactly when, where and how the substorm energization of plasmas proceeds in the magnetotail.

In the geospace environment, there are various boundaries between different plasma regimes which could often be described in a simple MHD way. However, kinetic processes in the collisionless plasmas may operate for the transfer and conversion of energy, momentum, and mass through these boundaries, and control the overall dynamics of the magnetospheric system. From this point of view, most important are the bow shock, the magnetopause and the plasma sheet boundary layer. Because of the narrowness of the boundaries and their mobility in space, the high-time-resolution measurement is needed to gain a deeper insight into the physics of these small-scale kinetic processes.

The Low-Energy Particle (LEP) experiment onboard GEOTAIL makes comprehensive observations of plasma and energetic electrons and ions with fine temporal resolution in the terrestrial magnetosphere (mainly magnetotail) and in the interplanetary medium. Emphasis in the instrument design is laid on the large geometrical factor to measure tenuous plasma in the magnetotail with sufficient counting statistics in the high-time-resolution measurement. In this paper, we describe the instrumentation and present some examples of the inflight measurements.

2. Instrument Description

2.1 Overview

The LEP instrument consists of three units of sensors (LEP-EA, LEP-SW and LEP-MS) and a common electronics (LEP-E). The Energy-per-charge Analyzers (LEP-EA) measure three-dimensional velocity distributions and their moments of hot plasmas (electrons and ions, separately and simultaneously) in the magnetosphere, while the Solar Wind ion analyzer (LEP-SW) measures three-dimensional velocity distribution and its moments of the solar wind ions with fine energy and angular resolutions. The energetic-ion Mass Spectrometer (LEP-MS) provides three-dimensional determinations of the ion composition. These sensor boxes are installed on the spacecraft, as shown schematically in Fig. 1. It should be noted that the spacecraft is spin-stabilized with ~20 rpm and the spin axis is perpendicular to the ecliptic plane within 5°. The measured and derived parameters are summarized in Table 1.

Figure 2 shows a functional block diagram of the LEP instrument. LEP-E consists of low-voltage electronic circuits, the functions of which are to control the energy, angular and mass sampling, to gather data from the sensors (LEP-EA, LEP-SW and LEP-MS), to perform the moment calculations from the data of the LEP-EA and LEP-SW sensors, and to interface the Data Handling Unit (DHU) for decoding the LEP commands, formatting the LEP data and monitoring the housekeeping data. It also outputs the trigger (burst) signal for the Plasma Wave Instrument (PWI) waveform capture when the result of the moment calculations exceeds a certain level specified by the command.

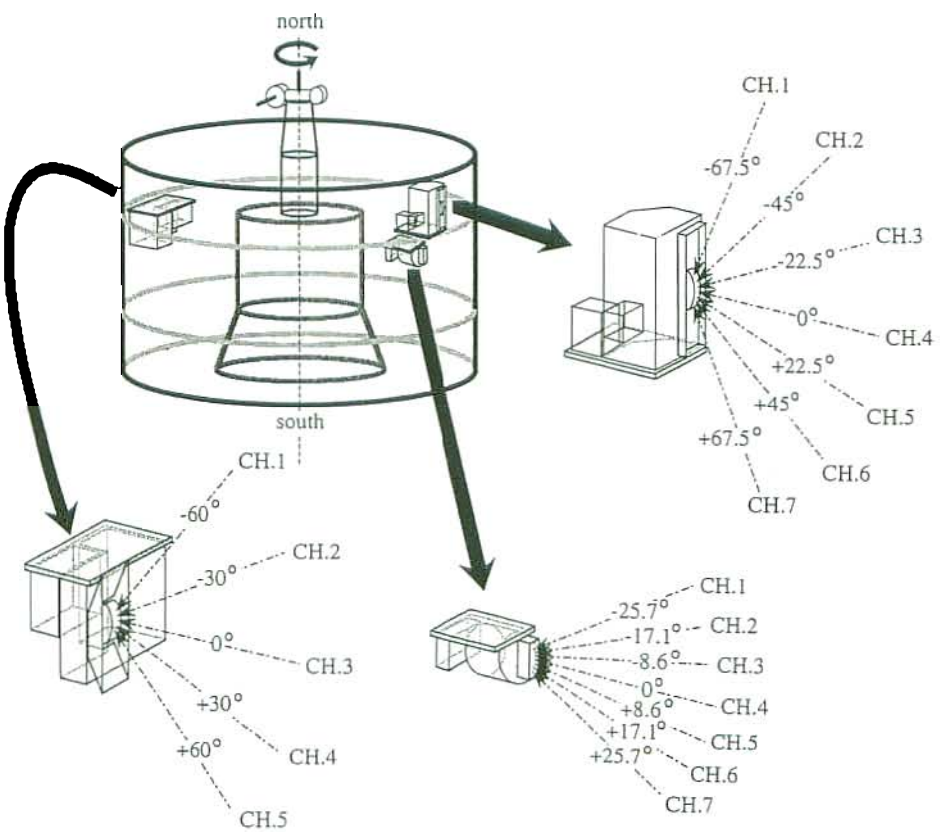

Fig. 1. Schematic drawing of three sensor units of LEP on the GEOTAIL satellite.

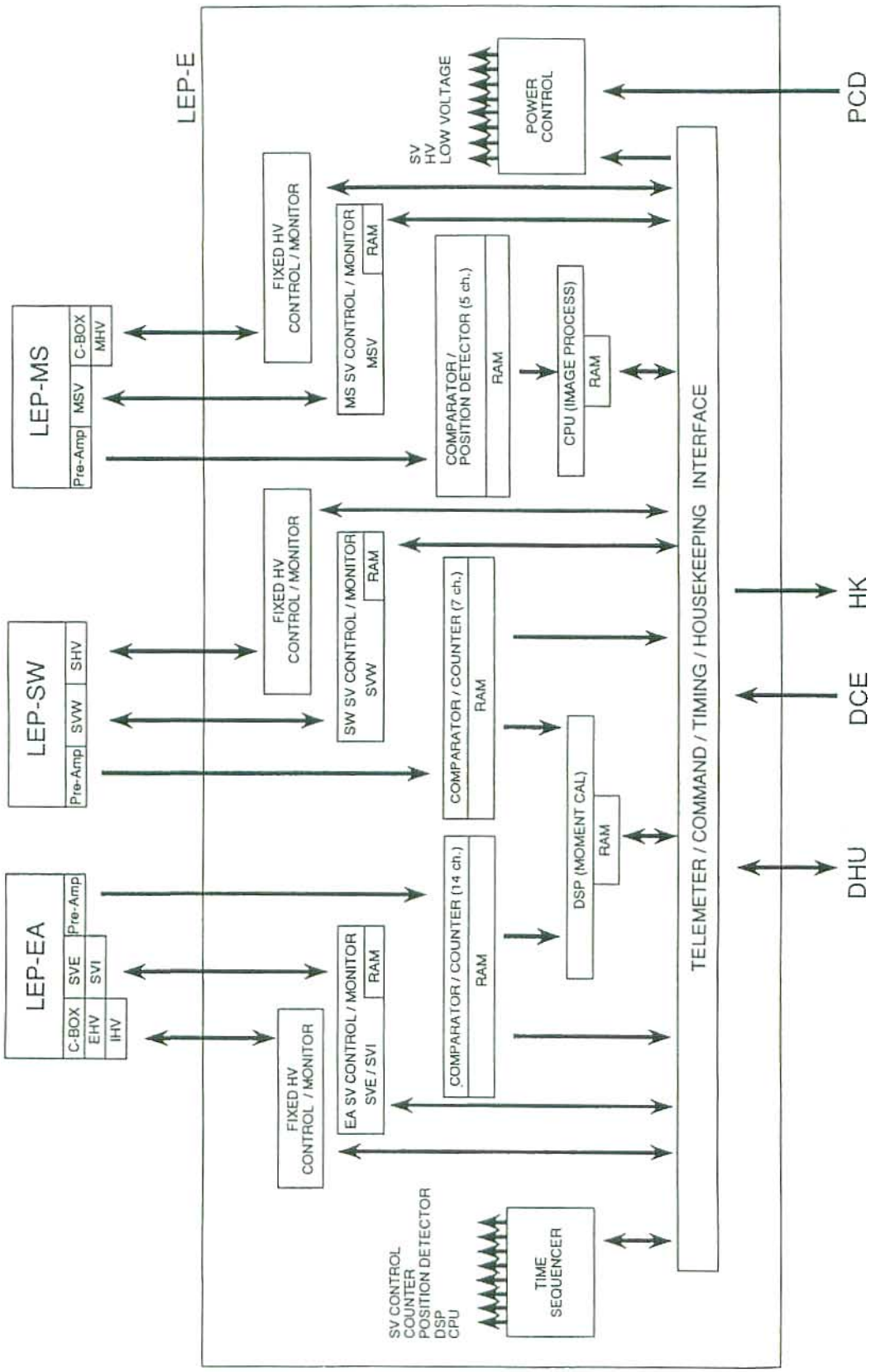

Fig. 2. Functional block diagram of LEP onboard the GEOTAIL satellite.

Table 1. Measured and derived parameters.

Sensor	Measured Parameters	Derived Parameters
EA SW	electron and ion count rates(*) for 32 energy steps, 16 azimuthal sectors and 7 elevation angles	three-dimensional velocity distribution functions of electrons and ions
	velocity moments for the electron and ion distribution functions up to the third order	number densities, flow velocities, pressure tensors and heat flux tensors of electrons and ions
	energy range EA-e : 8 eV - 38 keV EA-i : 32 eV/Q - 39 keV/Q SW-i : 140 eV/Q - 8 keV/Q	
MS	count rates(*) at 32 energy steps, 16 azimuthal sectors and 5 elevation angles for selected five ion species energy range: 0.1 - 25 keV/Q	three-dimensional velocity distributions and their moments for five ion species (H^+, He^{++}, He^+, O^{++}, O^+)

Note: The measured count rates can be directly converted into directional, differential energy intensities of electron and ion fluxes.

2.2 LEP-EA (LEP-EA-e and LEP-EA-i)

Figure 3 shows a schematic diagram of LEP-EA. It consists of two nested sets of quadrispherical electrostatic analyzers, the inner analyzer (LEP-EA-e) to measure electrons and the outer one (LEP-EA-i) to measure positive ions, separately and simultaneously over an energy range from several eV/Q to 43 keV/Q. The field of view for each quadrispherical analyzer covers $10° \times 145°$, where the longer dimension is parallel to the satellite spin axis. Both the inner and outer analyzers are operated with balanced potentials; that is, equal voltages with opposite polarities are applied to the plates in each analyzer. Charged particles with selected energy/charge and incident angles can travel through the analyzers and be measured. Seven channel electron multipliers (CEM's) and seven microchannel plates (MCP's) are used as electron detectors and ion detectors, respectively. These detectors (CEM's and MCP's) are placed at the positions corresponding to the incident elevation angles of 0°, ±22.5°, ±45.0° and ±67.5°, respectively (more exactly, see Table 2). As shown in Fig. 1, we use "Channel No. (CH.)" for each detector in LEP-EA as well as in LEP-SW and LEP-MS. Channel-1 (CH.1) denotes the detector looking toward the northmost elevation angle (+67.5°) and hence measuring the southward-going particles. Channel-4 (CH.4) is the center detector in the equator plane (roughly, ecliptic plane). Channel-7 (CH.7) is the detector opposite to Channel-1 and measures the northward-going particles.

Emphasis in the EA design is laid on the large geometrical factor to measure tenuous plasma in the magnetotail with sufficient counting statistics in the high-time resolution measurement. Figure 4 shows examples of the basic transmission characteristics for (a) EA-e Channel-4 sensor and (b) EA-i Channel-4 sensor, based on the preflight calibration experiment. As shown in Fig. 4, the energy and azimuthal (α) responses are strongly coupled with each other. This skewing is a well-known property for a quadrispherical electrostatic analyzer in general (e.g., Gosling *et al.*, 1978), and hence we have to be cautious in data

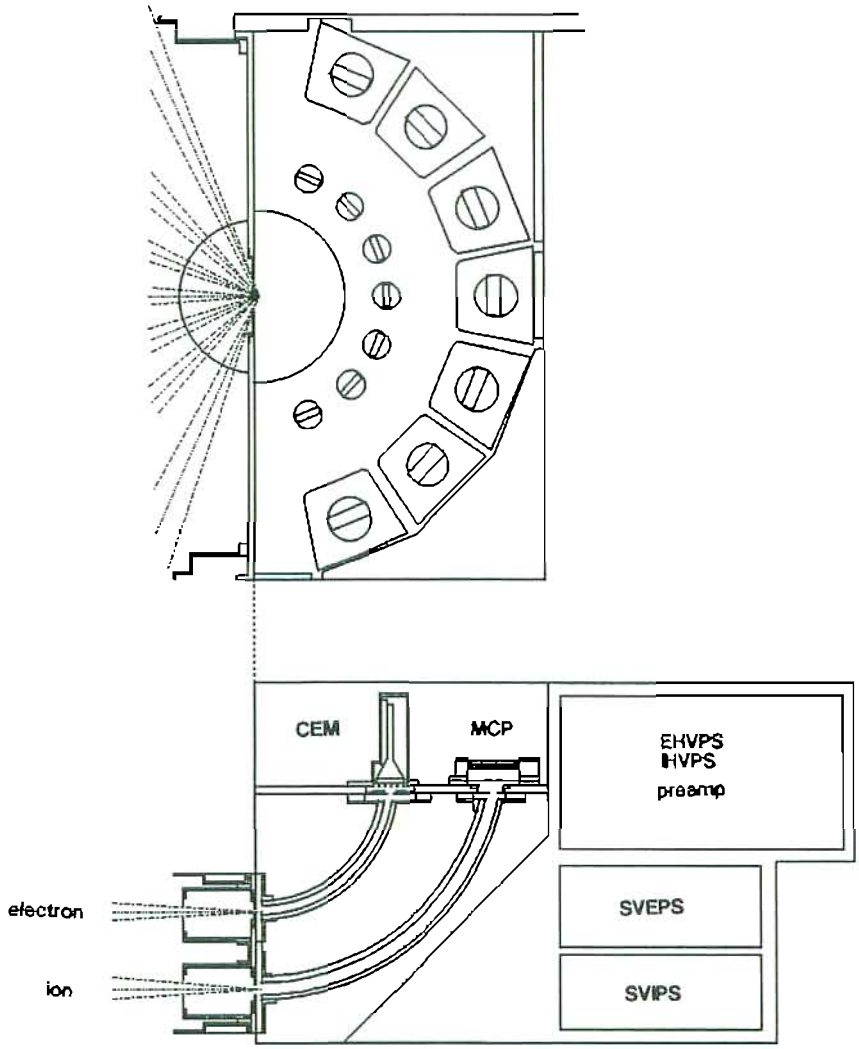

Fig. 3. Schematic diagram of LEP-EA.

processing when a monoenergetic beam is measured; that is, a deconvolution technique has to be done taking the transmission characteristics of the analyzer into account with assumption of the beam distribution function. In most cases, fortunately, the magnetospheric plasma has much wider spread in energy and angle compared to the analyzer response. Under the assumption that the incident particle flux is uniform within the energy and angular responses of the analyzer, the particle count C measured in a sampling time τ is given by

$$C = f(E, \theta, \alpha) \cdot G \cdot \Delta E \cdot \varepsilon \cdot \tau, \tag{1}$$

where $f(E, \theta, \alpha, t)$ is the differential particle flux in units of particles/(cm^2 s sr eV), and G and ΔE are the geometrical factor (cm^2 sr) and the energy band width (eV), respectively. ε is the detection efficiency, and it is estimated to be 0.65 by comparison of the density obtained by LEP with the plasma frequency observed by PWI. ΔE is proportional to the center energy, E; $\Delta E/E$ is constant (determined by the geometrical configuration of the electrostatic analyzer) over the entire energy range. The basic parameters of the instrument performance for the EA-e and EA-i sensors are summarized in Table 2, in which $\Delta\alpha$, $\Delta\theta$ and $\Delta\delta$ ($\equiv\Delta E/E$) represent the Full-Width at Half-Maximum (FWHM) in the α, θ, δ responses (for example, see Fig. 4), respectively, and the g-factor stands for $G{\cdot}\Delta\delta$.

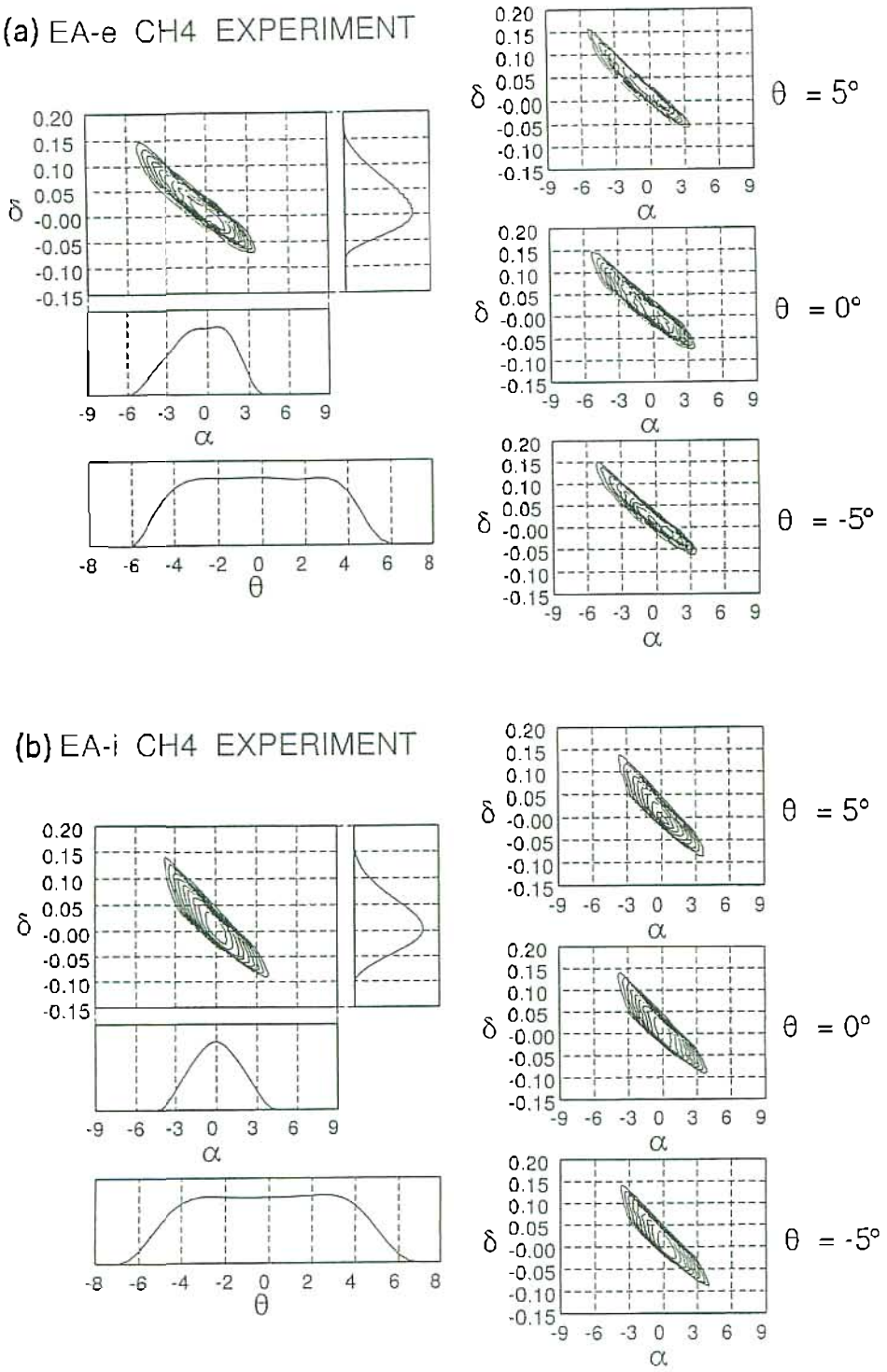

Fig. 4. (a) Transmission characteristics of the LEP-EA-e Channel-4 sensor. Three panels on the right hand side show relative transmissions (so-called, E-α response) in energy and azimuthal-angle coordinate for three elevation (θ) angles, in which δ is the normalized energy of particles ($(E - E_0)/E_0$; E_0 = center energy), and α is the azimuthal angle in the spacecraft frame with $\alpha = 0$ for the direction of normal incidence to the analyzer input plane. Contours are drawn every 10% of the maximum transmission in each panel. The upper-left panel shows the similar response integrated over elevation angles along with the energy (δ) and azimuthal-angle (α) responses. The elevational-angle (θ) response is also shown on the lower-left hand. The responses of δ, α and θ are obtained by integration of the transmission over two other parameters. (b) Similar to (a), except that this is the case for the LEP-EA-i Channel-4 sensor.

Table 2. Basic parameters of the instrument performance for the EA-e and EA-i sensors.

EA-e				
CHANNEL (DIRECTION)	$\Delta\alpha$ (FWHM)	$\Delta\theta$ (FWHM)	$\Delta\delta$ (FWHM)	g-factor ($cm^2 \cdot str \cdot eV/eV$)
CH1 (−66.0°)	8.4°	10.2°	14.0 %	1.68×10^{-4}
CH2 (−44.4°)	9.1°	8.6°	12.9 %	2.74×10^{-4}
CH3 (−22.1°)	9.1°	6.4°	12.6 %	3.58×10^{-4}
CH4 (0.0°)	9.4°	5.9°	12.4 %	4.08×10^{-4}
CH5 (22.0°)	9.0°	6.1°	12.5 %	3.93×10^{-4}
CH6 (44.2°)	9.5°	8.1°	12.6 %	3.08×10^{-4}
CH7 (65.7°)	8.4°	10.4°	13.6 %	1.80×10^{-4}

EA-i				
CHANNEL (DIRECTION)	$\Delta\alpha$ (FWHM)	$\Delta\theta$ (FWHM)	$\Delta\delta$ (FWHM)	g-factor ($cm^2 \cdot str \cdot eV/eV$)
CH1 (−65.5°)	6.8°	12.5°	15.2 %	6.74×10^{-4}
CH2 (−44.9°)	10.1°	7.9°	12.8 %	1.28×10^{-3}
CH3 (−22.2°)	10.3°	6.9°	11.7 %	1.45×10^{-3}
CH4 (0.0°)	10.2°	6.9°	11.6 %	1.51×10^{-3}
CH5 (22.3°)	10.1°	6.9°	11.7 %	1.44×10^{-3}
CH6 (44.7°)	10.4°	7.9°	12.4 %	1.21×10^{-3}
CH7 (65.6°)	6.7°	12.5°	15.0 %	6.10×10^{-4}

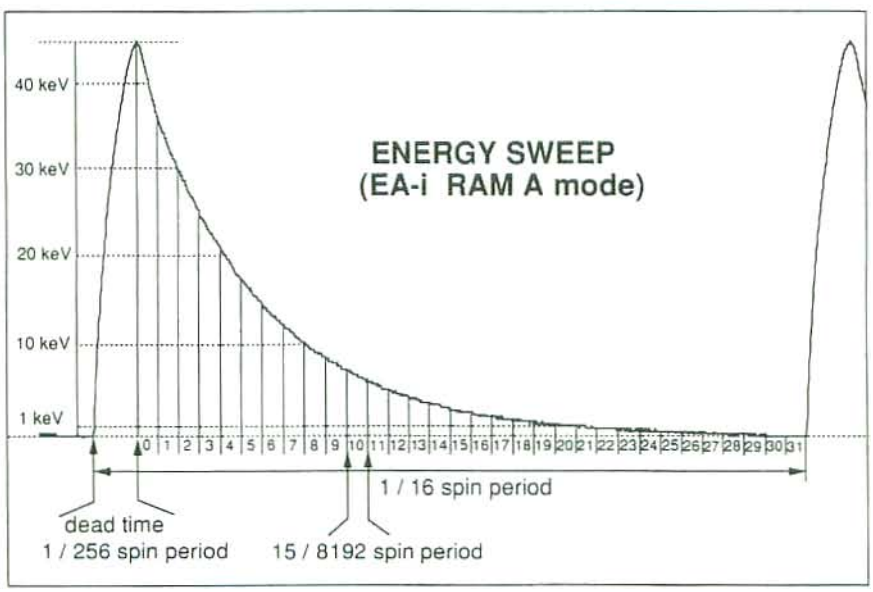

Fig. 5. Energy scanning waveform and its relation with the data samplings. The A-mode waveform in LEP-EA-i is shown here as an example.

The measurement is synchronized with the spin phase clock of the spacecraft. One spin period is divided into 16 azimuthal sectors, and in each sector, the electron and ion energies are scanned simultaneously and separately in selected modes. In any energy scanning mode the whole energy range is divided into 32 bins, as shown in Fig. 5. Thus, count rate data of dimension $32(E) \times 16(Az) \times 7(El)$ for both the electron and ion measurements are generated in one spin period. While the velocity moments are calculated onboard every spin period, the complete three-dimensional velocity distributions can only be obtained in a period of four spins owing to the telemetry constraints; the count data are accumulated during the four-spin period. Tables 3 and 4 shows the measured energies in EA-e and EA-i, respectively. Two energy scanning modes called RAM-A and RAM-B are prepared for EA-e and EA-i independently.

Table 3. Energy bins of EA-e.

	EA-e RAM A			EA-e RAM B		
STEP	E_0 (eV)	E_h (eV)	E_l (eV)	E_0 (eV)	E_h (eV)	E_l (eV)
0	3.815×10^4	4.163×10^4	3.488×10^4	7.621×10^3	8.491×10^3	6.813×10^3
1	3.197×10^4	3.488×10^4	2.922×10^4	6.115×10^3	6.813×10^3	5.466×10^3
2	2.678×10^4	2.922×10^4	2.448×10^4	4.906×10^3	5.466×10^3	4.386×10^3
3	2.244×10^4	2.448×10^4	2.051×10^4	3.937×10^3	4.386×10^3	3.519×10^3
4	1.880×10^4	2.051×10^4	1.719×10^4	3.159×10^3	3.519×10^3	2.824×10^3
5	1.575×10^4	1.719×10^4	1.440×10^4	2.535×10^3	2.824×10^3	2.266×10^3
6	1.320×10^4	1.440×10^4	1.207×10^4	2.034×10^3	2.266×10^3	1.818×10^3
7	1.106×10^4	1.207×10^4	1.011×10^4	1.632×10^3	1.818×10^3	1.459×10^3
8	9.266×10^3	1.011×10^4	8.471×10^3	1.309×10^3	1.459×10^3	1.170×10^3
9	7.765×10^3	8.471×10^3	7.098×10^3	1.051×10^3	1.170×10^3	9.392×10^2
10	6.506×10^3	7.098×10^3	5.948×10^3	8.430×10^2	9.392×10^2	7.536×10^2
11	5.452×10^3	5.948×10^3	4.984×10^3	6.764×10^2	7.536×10^2	6.047×10^2
12	4.568×10^3	4.984×10^3	4.177×10^3	5.427×10^2	6.047×10^2	4.852×10^2
13	3.828×10^3	4.177×10^3	3.500×10^3	4.355×10^2	4.852×10^2	3.893×10^2
14	3.208×10^3	3.500×10^3	2.933×10^3	3.494×10^2	3.893×10^2	3.124×10^2
15	2.689×10^3	2.933×10^3	2.458×10^3	2.804×10^2	3.124×10^2	2.506×10^2
16	2.253×10^3	2.458×10^3	2.060×10^3	2.250×10^2	2.506×10^2	2.011×10^2
17	1.888×10^3	2.060×10^3	1.726×10^3	1.805×10^2	2.011×10^2	1.614×10^2
18	1.582×10^3	1.726×10^3	1.447×10^3	1.448×10^2	1.614×10^2	1.295×10^2
19	1.326×10^3	1.447×10^3	1.212×10^3	1.162×10^2	1.295×10^2	1.039×10^2
20	1.111×10^3	1.212×10^3	1.016×10^3	9.325×10	1.039×10^2	8.336×10
21	9.313×10^2	1.016×10^3	8.515×10^2	7.482×10	8.336×10	6.689×10
22	7.806×10^2	8.515×10^2	7.137×10^2	6.004×10	6.689×10	5.367×10
23	6.542×10^2	7.137×10^2	5.981×10^2	4.817×10	5.367×10	4.306×10
24	5.199×10^2	5.981×10^2	4.853×10^2	3.865×10	4.306×10	3.455×10
25	4.518×10^2	4.853×10^2	4.172×10^2	3.101×10	3.455×10	2.772×10
26	3.838×10^2	4.172×10^2	3.491×10^2	2.488×10	2.772×10	2.225×10
27	3.157×10^2	3.491×10^2	2.810×10^2	1.997×10	2.225×10	1.785×10
28	2.477×10^2	2.810×10^2	2.130×10^2	1.602×10	1.785×10	1.432×10
29	1.754×10^2	2.130×10^2	1.343×10^2	1.286×10	1.432×10	1.149×10
30	9.320×10	1.343×10^2	7.660×10	1.031×10	1.149×10	9.221
31	6.000×10	7.660×10	4.340×10	8.276	9.221	7.399

Note: E_0 is the center energy of each bin. E_h and E_l are higher and lower boundaries of each bin.

Table 4. Energy bins of EA-i.

	EA-i RAM A			EA-i RAM B		
STEP	E_0 (eV)	E_h (eV)	E_l (eV)	E_0 (eV)	E_h (eV)	E_l (eV)
0	3.948×10^4	4.415×10^4	3.689×10^4	4.298×10^4	4.447×10^4	4.152×10^4
1	3.299×10^4	3.689×10^4	3.082×10^4	4.012×10^4	4.152×10^4	3.876×10^4
2	2.756×10^4	3.082×10^4	2.575×10^4	3.746×10^4	3.876×10^4	3.618×10^4
3	2.303×10^4	2.575×10^4	2.151×10^4	3.497×10^4	3.618×10^4	3.378×10^4
4	1.924×10^4	2.151×10^4	1.797×10^4	3.264×10^4	3.378×10^4	3.153×10^4
5	1.607×10^4	1.797×10^4	1.502×10^4	3.047×10^4	3.153×10^4	2.944×10^4
6	1.343×10^4	1.502×10^4	1.255×10^4	2.845×10^4	2.944×10^4	2.748×10^4
7	1.122×10^4	1.255×10^4	1.048×10^4	2.656×10^4	2.748×10^4	2.566×10^4
8	9.374×10^3	1.048×10^4	8.758×10^3	2.479×10^4	2.566×10^4	2.395×10^4
9	7.832×10^3	8.758×10^3	7.317×10^3	2.315×10^4	2.395×10^4	2.236×10^4
10	6.543×10^3	7.317×10^3	6.113×10^3	2.161×10^4	2.236×10^4	2.087×10^4
11	5.467×10^3	6.113×10^3	5.108×10^3	2.017×10^4	2.087×10^4	1.949×10^4
12	4.567×10^3	5.108×10^3	4.267×10^3	1.883×10^4	1.949×10^2	1.819×10^4
13	3.816×10^3	4.267×10^3	3.565×10^3	1.758×10^4	1.819×10^4	1.698×10^4
14	3.188×10^3	3.565×10^3	2.979×10^3	1.641×10^4	1.698×10^4	1.586×10^4
15	2.664×10^3	2.979×10^3	2.489×10^3	1.532×10^4	1.586×10^4	1.480×10^4
16	2.226×10^3	2.489×10^3	2.079×10^3	1.430×10^4	1.480×10^4	1.382×10^4
17	1.859×10^3	2.079×10^3	1.737×10^3	1.335×10^4	1.382×10^4	1.290×10^4
18	1.554×10^3	1.737×10^3	1.451×10^3	1.247×10^4	1.290×10^4	1.204×10^4
19	1.298×10^3	1.451×10^3	1.213×10^3	1.164×10^4	1.204×10^4	1.124×10^4
20	1.084×10^3	1.213×10^3	1.013×10^3	1.087×10^4	1.124×10^4	1.050×10^4
21	9.061×10^2	1.013×10^3	8.465×10^2	1.014×10^4	1.050×10^4	9.799×10^3
22	7.570×10^2	8.465×10^2	7.073×10^2	9.470×10^3	9.799×10^3	9.148×10^3
23	6.325×10^2	7.073×10^2	5.909×10^2	8.841×10^3	9.148×10^3	8.540×10^3
24	5.681×10^2	5.909×10^2	5.276×10^2	8.254×10^3	8.540×10^3	7.973×10^3
25	4.872×10^2	5.276×10^2	4.467×10^2	7.705×10^3	7.973×10^3	7.443×10^3
26	4.062×10^2	4.467×10^2	3.658×10^2	7.193×10^3	7.443×10^3	6.949×10^3
27	3.253×10^2	3.658×10^2	2.848×10^2	6.716×10^3	6.949×10^3	6.487×10^3
28	2.444×10^2	2.848×10^2	2.039×10^2	6.270×10^3	6.487×10^3	6.057×10^3
29	1.634×10^2	2.039×10^2	1.229×10^2	5.853×10^3	6.057×10^3	5.654×10^3
30	8.247×10	1.229×10^2	4.200×10	5.464×10^3	5.654×10^3	5.278×10^3
31	3.169×10	4.200×10	2.139×10	5.101×10^3	5.278×10^3	4.928×10^3

Note: E_0 is the center energy of each bin. E_h and E_l are higher and lower boundaries of each bin.

2.3 LEP-SW

Since the geometrical factor of LEP-EA-i is too large to measure the solar wind ions (especially, protons), it is supplemented by LEP-SW with a smaller geometrical factor to measure the solar wind ions in the energy range from 0.1 to 8 keV/Q. The measurement principle and method of LEP-SW are quite similar to those of LEP-EA-i, however LEP-SW uses a 270°-spherical electrostatic analyzer with the field of view of 5° × 60°. Figure 6 shows schematically the principle of the 270°-spherical analyzer, which has been proved to be very useful for the solar wind measurement onboard PLANET-A (Suisei) spacecraft (Mukai *et al.*, 1987). Figure 7 shows examples of the transmission characteristics for the SW Channel-4 sensor. It is clearly seen that the angular and energy responses of the SW sensor are narrower with less

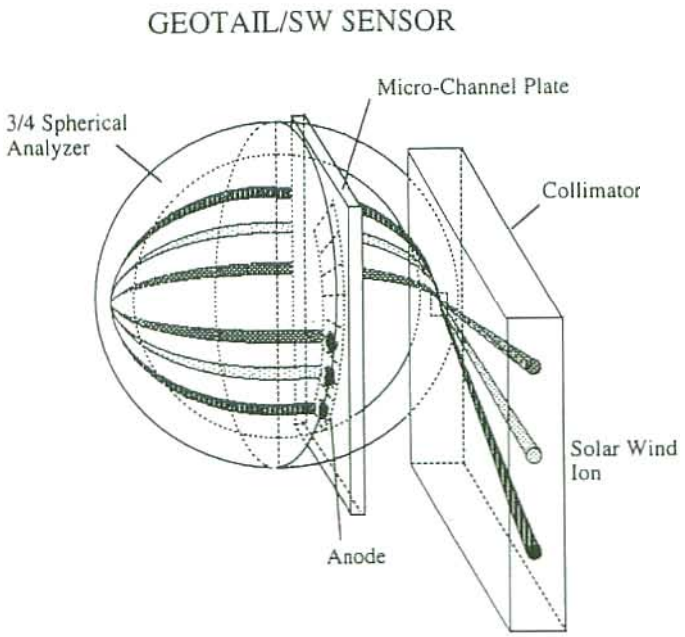

Fig. 6. Measurement principle of the 270° spherical electrostatic analyzer in LEP-SW.

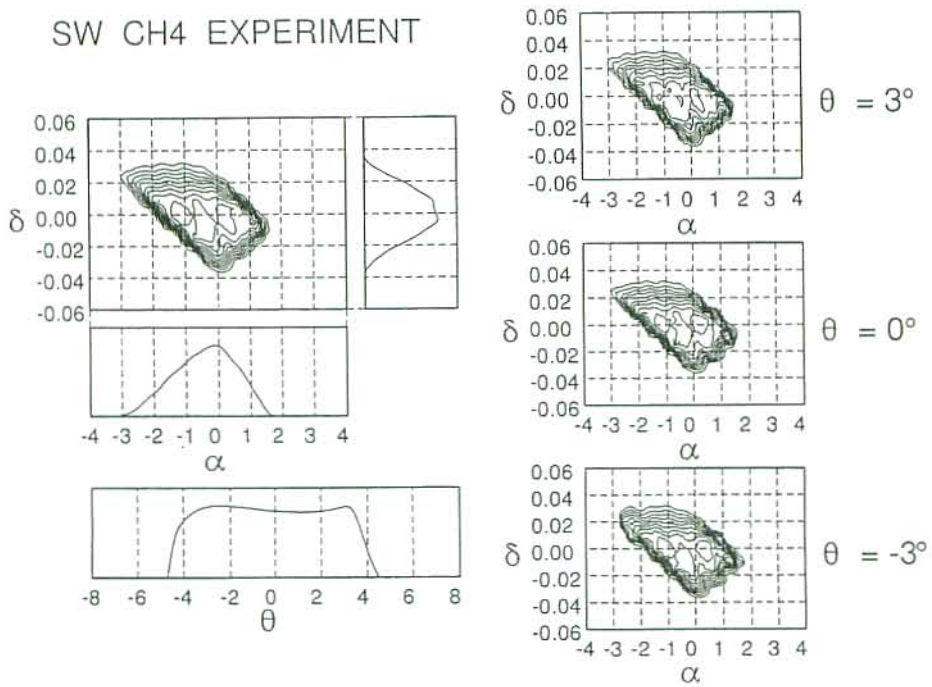

Fig. 7. Similar to Fig. 5(a), except that this is the case for the LEP-SW Channel-4 sensor.

skewing, compared to those of the EA-i sensor shown in Fig. 4, indicating the fine angular and energy resolutions. Equation (1) is also applicable for the LEP-SW sensor, where the efficiency ε is estimated to be 0.75. The basic performance parameters of LEP-SW are summarized in Table 5.

The operation of LEP-SW is similar to that of LEP-EA, except that it is carried out within spin phase of ±45° from the direction toward the sun. The azimuthal sectors are also divided into sixteen, and count rate data of dimension $32(E) \times 16(Az) \times 7(El)$ are generated in one spin period. Table 6 shows the measured

energies for LEP-SW. While the velocity moments are calculated onboard every spin period, the complete three-dimensional velocity distributions can only be obtained in a period of four spins owing to the telemetry constraints. In the SW operation, the count data for the first of the four spins are only transmitted to the ground.

2.4 LEP-MS

LEP-MS is an energetic-ion mass-spectrometer, which provides three-dimensional determinations of the ion composition in 32 steps over the energy range of 0.1 to 25 keV/Q. Figure 8 shows a schematic view of LEP-MS. It is composed of an inlet collimator, tandem (spherical and poloidal) electrostatic

Table 5. Basic parameters of the instrument performance for the SW sensor.

SW				
CHANNEL (DIRECTION)	$\Delta\alpha$ (FWHM)	$\Delta\theta$ (FWHM)	$\Delta\delta$ (FWHM)	g-factor ($cm^2 \cdot str \cdot eV/eV$)
CH1 (−25.2°)	2.5°	8.0°	3.7 %	9.87×10^{-6}
CH2 (−17.2°)	2.5°	8.9°	3.9 %	1.08×10^{-5}
CH3 (−8.6°)	2.5°	8.3°	3.9 %	1.14×10^{-5}
CH4 (0.0°)	2.5°	8.3°	4.0 %	1.14×10^{-5}
CH5 (8.7°)	2.6°	8.4°	4.2 %	1.14×10^{-5}
CH6 (17.3°)	2.7°	8.6°	4.5 %	1.08×10^{-5}
CH7 (26.0°)	2.8°	9.0°	4.4 %	9.87×10^{-6}

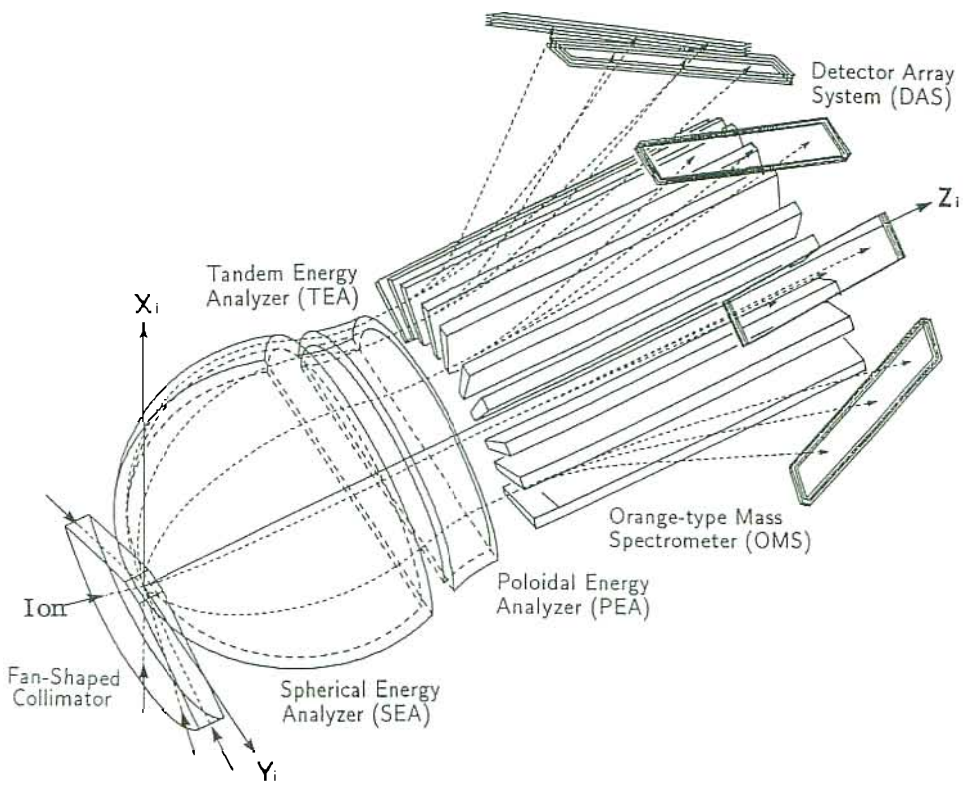

Fig. 8. Three-dimensional view of the LEP-MS spectrometer and several ion trajectories (dotted curves with arrows) with different values of mass-per-charge in five elevational angles of particle incidence.

analyzers, an orange-type magnetic analyzer and MCP detectors. Five MCP detectors are placed at the positions corresponding to the elevation angles of 0°, ±30° and ±60°. Each MCP is used as a position-sensitive detector which can provide the 64 point ion mass spectrum simultaneously. An onboard microprocessor is used for reducing the raw 64-point spectrum to the counts for five selectable ion species (nominally, H^+, He^{2+}, He^+, O^{2+}, and O^+), background counts and total counts. Thus LEP-MS can determine three-dimensional distributions of different ion species simultaneously. On the other hand, the LEP-MS operation and the relevant onboard processing of the data are complicated, compared to the other sensor units, and will be described elsewhere.

Table 6. Energy bins of SW.

	SW RAM A			SW RAM B		
STEP	E_0 (eV)	E_h (eV)	E_l (eV)	E_0 (eV)	E_h (eV)	E_l (eV)
0	8.034×10^3	8.308×10^3	7.811×10^3	3.992×10^3	4.089×10^3	3.894×10^3
1	7.548×10^3	7.811×10^3	7.270×10^3	3.760×10^3	3.894×10^3	3.601×10^3
2	6.829×10^3	7.270×10^3	6.453×10^3	3.408×10^3	3.601×10^3	3.223×10^3
3	6.104×10^3	6.453×10^3	5.768×10^3	3.052×10^3	3.223×10^3	2.887×10^3
4	5.456×10^3	5.768×10^3	5.156×10^3	2.734×10^3	2.887×10^3	2.586×10^3
5	4.877×10^3	5.156×10^3	4.609×10^3	2.449×10^3	2.586×10^3	2.317×10^3
6	4.359×10^3	4.609×10^3	4.119×10^3	2.194×10^3	2.317×10^3	2.075×10^3
7	3.897×10^3	4.119×10^3	3.682×10^3	1.965×10^3	2.075×10^3	1.859×10^3
8	3.483×10^3	3.682×10^3	3.291×10^3	1.760×10^3	1.859×10^3	1.665×10^3
9	3.113×10^3	3.291×10^3	2.942×10^3	1.576×10^3	1.665×10^3	1.491×10^3
10	2.783×10^3	2.942×10^3	2.630×10^3	1.412×10^3	1.491×10^3	1.336×10^3
11	2.487×10^3	2.630×10^3	2.351×10^3	1.265×10^3	1.336×10^3	1.196×10^3
12	2.223×10^3	2.351×10^3	2.101×10^3	1.133×10^3	1.196×10^3	1.072×10^3
13	1.987×10^3	2.101×10^3	1.878×10^3	1.015×10^3	1.072×10^3	9.598×10^2
14	1.776×10^3	1.878×10^3	1.679×10^3	9.089×10^2	9.598×10^2	8.597×10^2
15	1.588×10^3	1.679×10^3	1.500×10^3	8.141×10^2	8.597×10^2	7.701×10^2
16	1.419×10^3	1.500×10^3	1.341×10^3	7.292×10^2	7.701×10^2	6.898×10^2
17	1.269×10^3	1.341×10^3	1.199×10^3	6.531×10^2	6.898×10^2	6.178×10^2
18	1.134×10^3	1.199×10^3	1.072×10^3	5.850×10^2	6.178×10^2	5.534×10^2
19	1.014×10^3	1.072×10^3	9.579×10^2	5.240×10^2	5.534×10^2	4.957×10^2
20	9.061×10^2	9.579×10^2	8.562×10^2	4.694×10^2	4.957×10^2	4.440×10^2
21	8.100×10^2	8.562×10^2	7.653×10^2	4.204×10^2	4.440×10^2	3.977×10^2
22	7.239×10^2	7.653×10^2	6.841×10^2	3.766×10^2	3.977×10^2	3.562×10^2
23	6.471×10^2	6.841×10^2	6.115×10^2	3.373×10^2	3.562×10^2	3.191×10^2
24	5.784×10^2	6.115×10^2	5.466×10^2	3.021×10^2	3.191×10^2	2.858×10^2
25	5.170×10^2	5.466×10^2	4.885×10^2	2.706×10^2	2.858×10^2	2.560×10^2
26	4.621×10^2	4.885×10^2	4.367×10^2	2.424×10^2	2.560×10^2	2.293×10^2
27	4.131×10^2	4.367×10^2	3.903×10^2	2.171×10^2	2.293×10^2	2.054×10^2
28	3.692×10^2	3.903×10^2	3.489×10^2	1.945×10^2	2.054×10^2	1.840×10^2
29	3.300×10^2	3.489×10^2	3.119×10^2	1.742×10^2	1.840×10^2	1.648×10^2
30	2.950×10^2	3.119×10^2	2.788×10^2	1.560×10^2	1.648×10^2	1.476×10^2
31	2.637×10^2	2.788×10^2	2.492×10^2	1.398×10^2	1.476×10^2	1.322×10^2

Note: E_0 is the center energy of each bin. E_h and E_l are higher and lower boundaries of each bin.

2.5 Onboard data processing

The GEOTAIL satellite has two separate editors onboard, with bit rates of 65,536 bps in Editor-A and 16,384 bps in Editor-B for transmission of the whole science data along with the spacecraft common status, housekeeping data and attitude data, in which the LEP science data occupy 13,824 bps and 2,048 bps in the Editor-A and Editor-B formats, respectively. The contents of the LEP science data are different between Editor-A and Editor-B. Although the three-dimensional measurements in LEP-EA and LEP-SW are completed every one spin period, the raw data of the three-dimensional distributions are transmitted in a period of four spins in the Editor-A format, while in the Editor-B format either the two-dimensional data with the same time resolution as in the Editor-A or the three-dimensional data with coarser time resolution are transmitted, and at the same time, are stored in the tape recorders on the basis of 24-hour continuous recording. Results of the onboard moment calculations are included in both the Editor-A and Editor-B format. In the normal operation, the Editor-A data are only acquired in Usuda Deep Space Center (UDSC) in Japan, while the Editor-B stored data in the tape recorders are dumped over the NASA/JPL/DSN stations.

The raw count data for EA (3-D), EA (2-D), SW (3-D), SW (2-D), and MS (total) consist of 12, 16, 8, 12, and 12 bits, respectively. These raw count data are compressed onboard into 8-bit data. Conversion from the 8-bit data to the raw 12-bit data C is given by

$$C = D \qquad \text{for } S = 0, \tag{2}$$

and

$$C = 2^{S-1} \cdot (D + 32) \qquad \text{for } S \neq 0, \tag{3}$$

where S and D are the upper three and the lower five bits in the 8-bit PCM data. For the 16-bit raw data of EA (2-D),

$$C = D \qquad \text{for } S = 0, \tag{4}$$

and

$$C = 2^{S-1} \cdot (D + 16) \qquad \text{for } S \neq 0, \tag{5}$$

where S and D are the upper four and the lower four bits, respectively.

The velocity moments are calculated from the particle counts C_{ijk} at energy step E_i ($i = 1, 2, \ldots, 32$), azimuthal sector ϕ_j ($j = 1, 2, \ldots, 16$; ϕ also depends on i), and elevation angle θ_k ($k = 1, 2, \ldots, 7$):

$$C_{ijk} = C_{ijk} \cdot \alpha_k, \tag{6}$$

$$n = \sum_{i,j} \frac{1}{v_i} \sum_{k=1}^{7} C_{ijk}, \tag{7}$$

$$nV_x = \sum_{i,j} \cos\phi_{ij} \sum_{k=1}^{7} C_{ijk} \cos\theta_k, \tag{8}$$

$$nV_y = \sum_{i,j} \sin\phi_{ij} \sum_{k=1}^{7} C_{ijk} \cos\theta_k, \tag{9}$$

$$nV_z = \sum_{i,j} \sum_{k=1}^{7} C_{ijk} \sin\theta_k, \tag{10}$$

$$P_{xx} = \sum_{i,j} v_i \cos^2\phi_{ij} \sum_{k=1}^{7} C_{ijk} \cos^2\theta_k, \tag{11}$$

$$P_{yy} = \sum_{i,j} v_i \sin^2\phi_{ij} \sum_{k=1}^{7} C_{ijk} \cos^2\theta_k, \tag{12}$$

$$P_{zz} = \sum_{i,j} v_i \sum_{k=1}^{7} C_{ijk} \sin^2\theta_k, \tag{13}$$

$$P_{xy} = \sum_{i,j} v_i \cos\phi_{ij} \sin\phi_{ij} \sum_{k=1}^{7} C_{ijk} \cos^2\theta_k, \tag{14}$$

$$P_{yz} = \sum_{i,j} v_i \sin\phi_{ij} \sum_{k=1}^{7} C_{ijk} \cos\theta_k \sin\theta_k, \tag{15}$$

$$P_{zx} = \sum_{i,j} v_i \cos\phi_{ij} \sum_{k=1}^{7} C_{ijk} \cos\theta_k \sin\theta_k, \tag{16}$$

$$H_{xxx} = \sum_{i,j} v_i^2 \cos^3\phi_{ij} \sum_{k=1}^{7} C_{ijk} \cos^3\theta_k, \tag{17}$$

$$H_{xyy} = \sum_{i,j} v_i^2 \cos\phi_{ij} \sin^2\phi_{ij} \sum_{k=1}^{7} C_{ijk} \cos^3\theta_k, \tag{18}$$

$$H_{xzz} = \sum_{i,j} v_i^2 \cos\phi_{ij} \sum_{k=1}^{7} C_{ijk} \cos\theta_k \sin^2\theta_k, \tag{19}$$

$$H_{yyy} = \sum_{i,j} v_i^2 \sin^3\phi_{ij} \sum_{k=1}^{7} C_{ijk} \cos^3\theta_k, \tag{20}$$

$$H_{yxx} = \sum_{i,j} v_i^2 \sin\phi_{ij} \cos^2\phi_{ij} \sum_{k=1}^{7} C_{ijk} \cos^3\theta_k, \tag{21}$$

$$H_{yzz} = \sum_{i,j} v_i^2 \sin\phi_{ij} \sum_{k=1}^{7} C_{ijk} \cos\theta_k \sin^2\theta_k, \tag{22}$$

$$H_{zzz} = \sum_{i,j} v_i^2 \sum_{k=1}^{7} C_{ijk} \sin^3\theta_k, \tag{23}$$

$$H_{zxx} = \sum_{i,j} v_i^2 \cos^2\phi_{ij} \sum_{k=1}^{7} C_{ijk} \sin\theta_k \cos^2\theta_k, \tag{24}$$

$$H_{zyy} = \sum_{i,j} v_i^2 \sin^2\phi_{ij} \sum_{k=1}^{7} C_{ijk} \sin\theta_k \cos^2\theta_k, \tag{25}$$

$$H_{xyz} = \sum_{i,j} v_i^2 \cos\phi_{ij} \sin\phi_{ij} \sum_{k=1}^{7} C_{ijk} \sin\theta_k \cos^2\theta_k, \tag{26}$$

where n, V, P and H are number density, bulk velocity, pressure tensor and heat flux tensor in the spacecraft coordinate system, respectively. Particle velocity v_i can be determined from E_i, if the mass and charge state of particles are specified; actually, proton is assumed for the positive ion species. α_k is the correction factor including the geometrical factor, the detection efficiency and the energy width in performing the integration. It is also noted that the number densities and bulk velocities for the EA-e and EA-i data are calculated separately in four azimuthal sectors and in two energy ranges, of which the boundary is

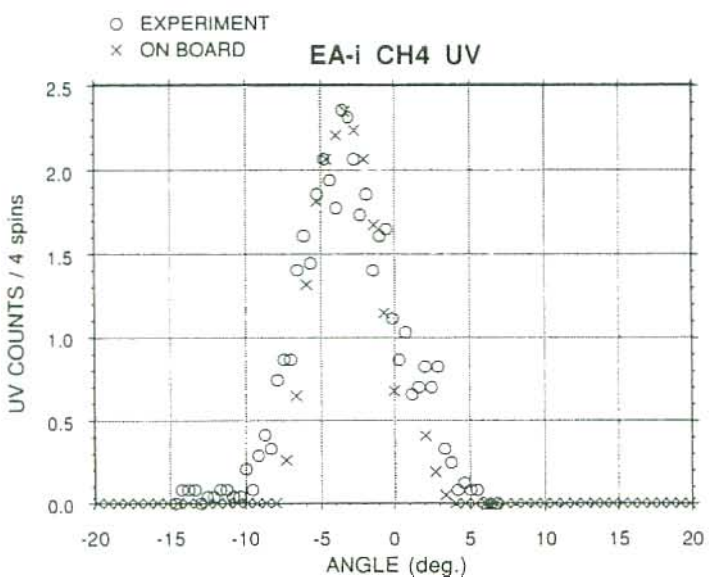

Fig. 9. Comparison of the solar EUV background in LEP-EA-i Channel-4 between the inflight data and the preflight experiment using a D_2 lamp. The abscissa is the azimuthal phase angle with respect to the solar direction, and the ordinate is the count/sample in four spins. The flight data were obtained in the A-mode energy scanning. It should be noted that the solar EUV background for detectors other than Channel-4 is reduced to much lower levels. A fairly good agreement between both data suggests that the preflight assessment of this background was reasonable, and the background noise can be easily subtracted from raw data.

specified by a command, so that a bidirectional streaming flow can be identified unambiguously. While the velocity moments are calculated in 32-bit floating calculations by a dedicated digital signal processor, they are compressed into 8-bit data in a sophisticated floating code.

3. Inflight Performance and Initial Results

The initial turn-on test of the high-voltage power supplies was successfully carried out on August 17 and 20, 1992, and thereafter the LEP instrument became operational. However, part of the low-voltage electronics in LEP-E was latched up suddenly on August 22, and the operation of the LEP instrument became suspended unfortunately until the recent recovery on September 1, 1993. Though the initial operation was limited in a short period of time (in total, ~6 hours) on August 20 and 22, 1992, the inflight performance of the LEP instrument was perfectly as expected, and exciting data were obtained on the plasma dynamics in the mid-tail region.

Quality of the data is determined by subtraction of background noise, which is contained, more or

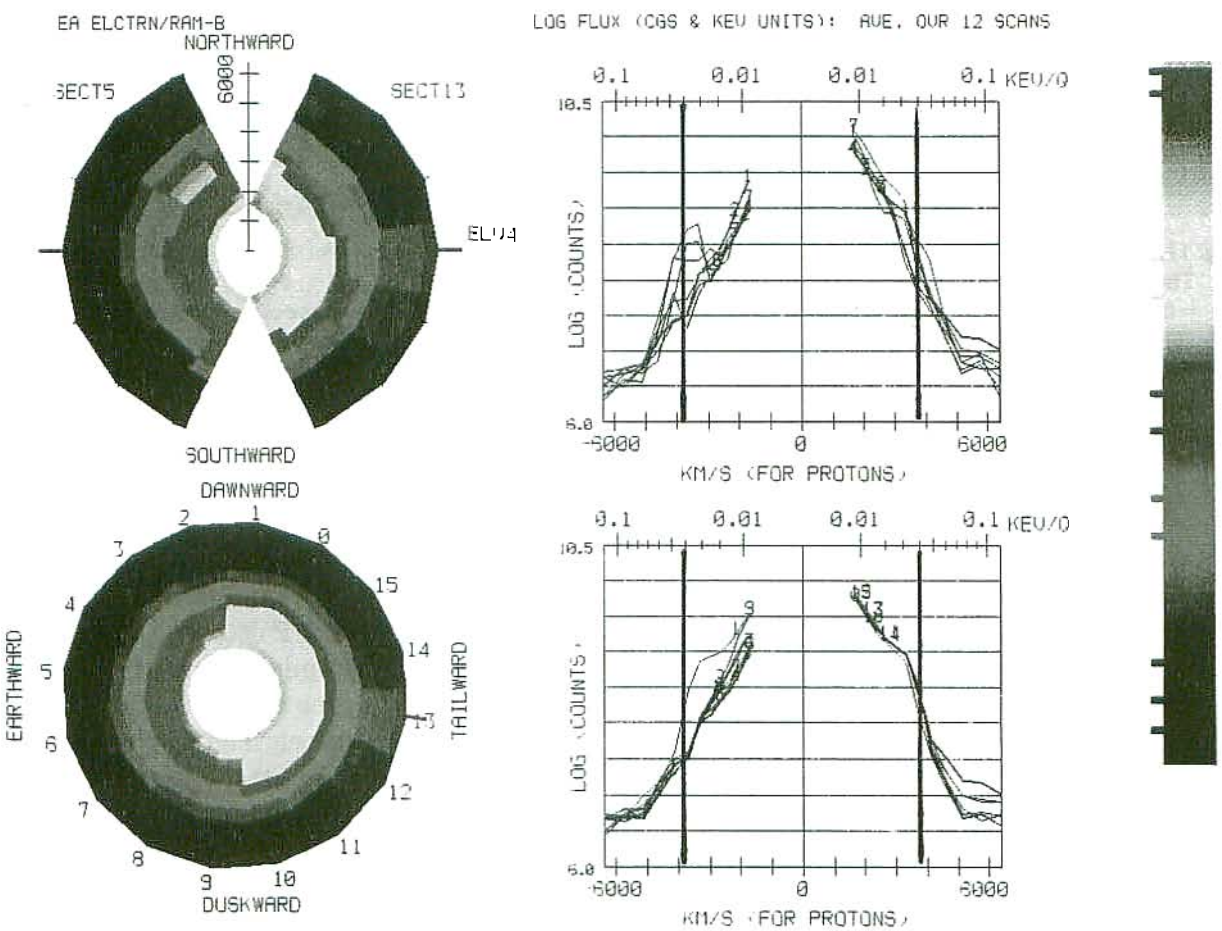

Fig. 10. Three-dimensional distribution of electrons in the lobe region observed during the time interval of 1251:46–1254:22 UT on August 22, 1992 (see also Fig. 14). The radial scale in the left-hand panels and the abscissa scale in the right-hand panels are equal, and represent the electron velocity in km/s. Here the data in a lower energy range below 116 eV are only displayed to make the nature of the spacecraft photoelectrons clear. The number flux in unit of $(cm^2\ s\ sr\ eV)^{-1}$ on a logarithmic scale are coded by color in the left-hand panels and are shown by the ordinates in the right-hand panels. In this example, the spacecraft potential is estimated as 40 volt from the cutoff of the spacecraft photoelectrons as shown by vertical lines on the right hand panels.

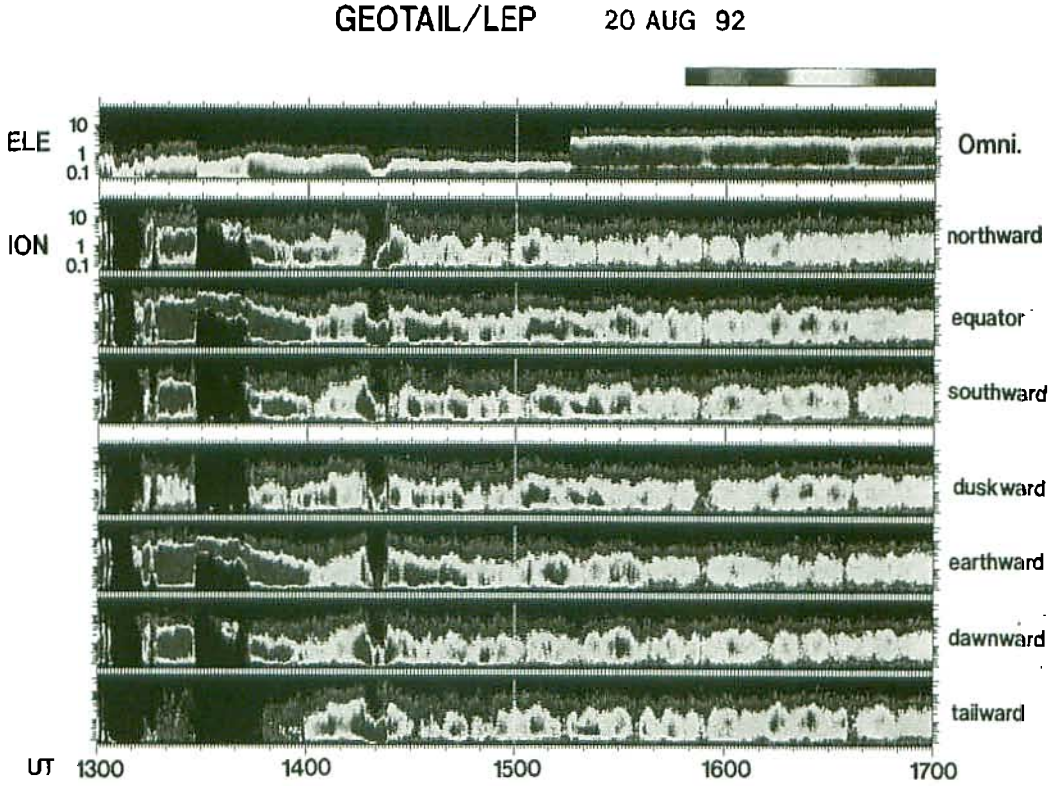

Fig. 11. Energy-time spectrograms of electrons and ions observed during the time interval of 1300 to 1700 UT on August 20. The spacecraft was located in the mid-tail region (mostly in the plasma sheet); $X_{GSM} = -60$ Re, $Y_{GSM} = +12$ Re, and $Z_{GSM} = 0$ Re. From top to bottom, data of the omnidirectional electrons, and the ion data in three elevational directions and in four azimuthal directions are shown. The energy scanning mode for the electron measurement was changed at 1516 UT (see arrow) from the A-mode to the B-mode. The energy scale in the electron data is valid only for the A-mode. It is noted that the maximum count data at a given energy and time are displayed in each specified direction; for example, the northward data show the maximum of the data of Channel-6 and Channel-7 in all azimuthal sectors, and the tailward data are the maximum of the raw data in seven channels (elevational directions) and four azimuthal sectors centered at the tailward direction.

less, inevitably in raw count data. The major sources for the background noise are electrical interference, high-energy particle penetration, thermal emission inside the CEM and MCP detectors, and solar EUV radiation. While the first three sources are generally distributed randomly in time, the solar EUV background is dominant only when it enters into the field of view of the analyzers. Figure 9 shows comparison of the solar EUV background in the LEP-EA-i sensor between the inflight data and the preflight experiment using a D_2 EUV lamp. The solar EUV background is negligibly small in the LEP-SW sensor, in which the 270° spherical analyzer is used and hence the ray path from the inlet aperture to the MCP detector is very long. The EA-e data also contain non-ambient electrons in lower energies, which arise from the spacecraft photoelectrons emitted by the solar EUV radiation. These photoelectrons are turned back to the spacecraft, because the electric potential of the spacecraft is positive with respect to the ambient plasma potential. Hence the photoelectron energy spectrum, especially the cut-off energy, is a useful indication of the spacecraft potential, as shown in Fig. 10.

Figure 11 shows energy-time spectrograms of the LEP-EA data observed on August 20, in which the ion data are sorted by different elevational and azimuthal angles, and the electron data represent the omnidirectional energy flux. The GEOTAIL satellite was located in the mid-tail region; $X_{GSM} = -60$ Re, $Y_{GSM} = +12$ Re, $Z_{GSM} = 0$ Re. During the observation, the geomagnetic conditions were quiet ($K_p = 2_0$), though a substorm (Pi-2 onset) took place two hours prior to the beginning of the observation (Yumoto,

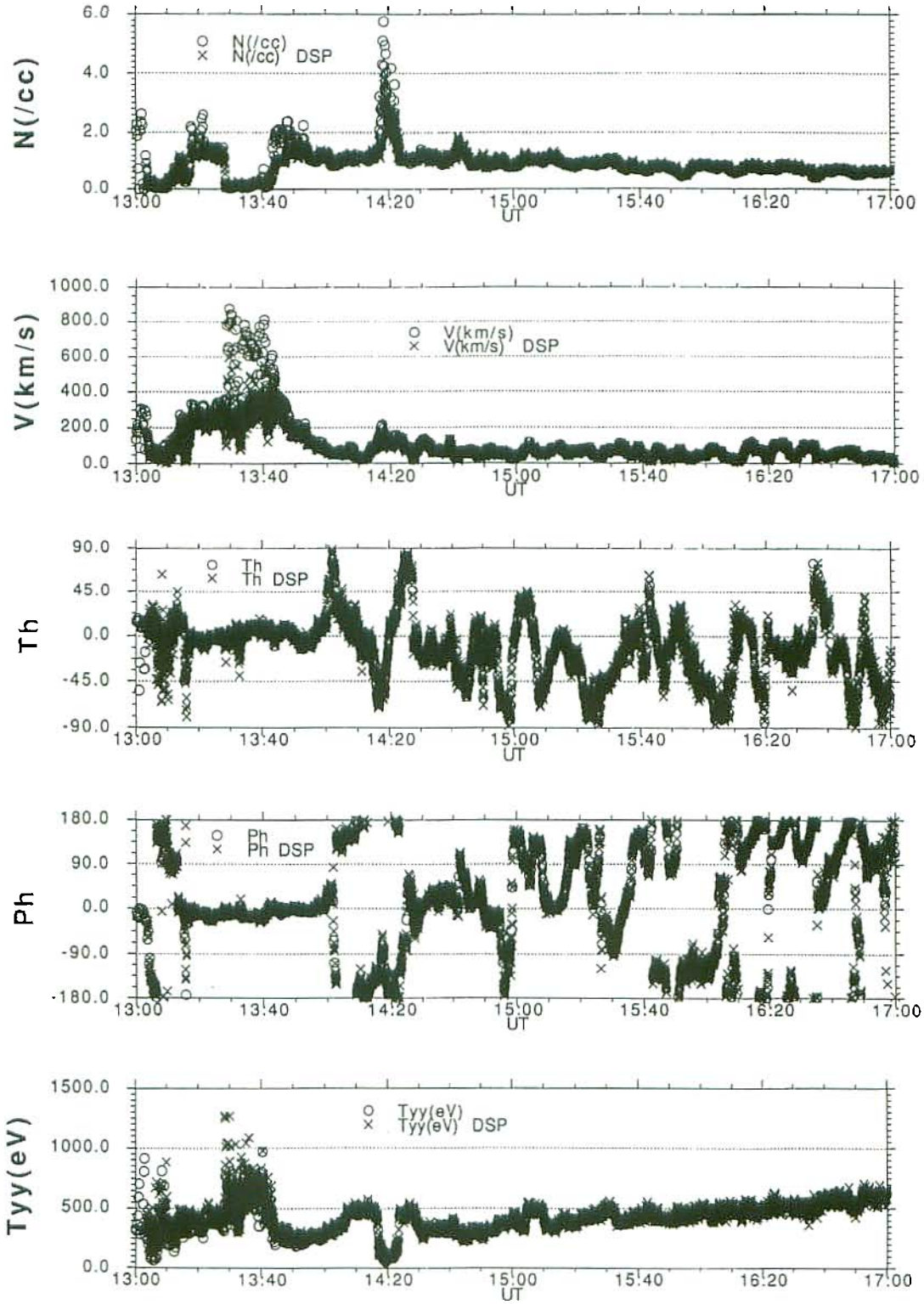

Fig. 12. From top to bottom, density, magnitude, elevation and azimuthal angles of the bulk velocity, and perpendicular temperature of ions during the same time interval as shown in Fig. 11. The results obtained by the onboard moment calculation (marked by asterisks) and those (marked by open circles) calculated from the three-dimensional velocity distributions on the ground are shown for comparison.

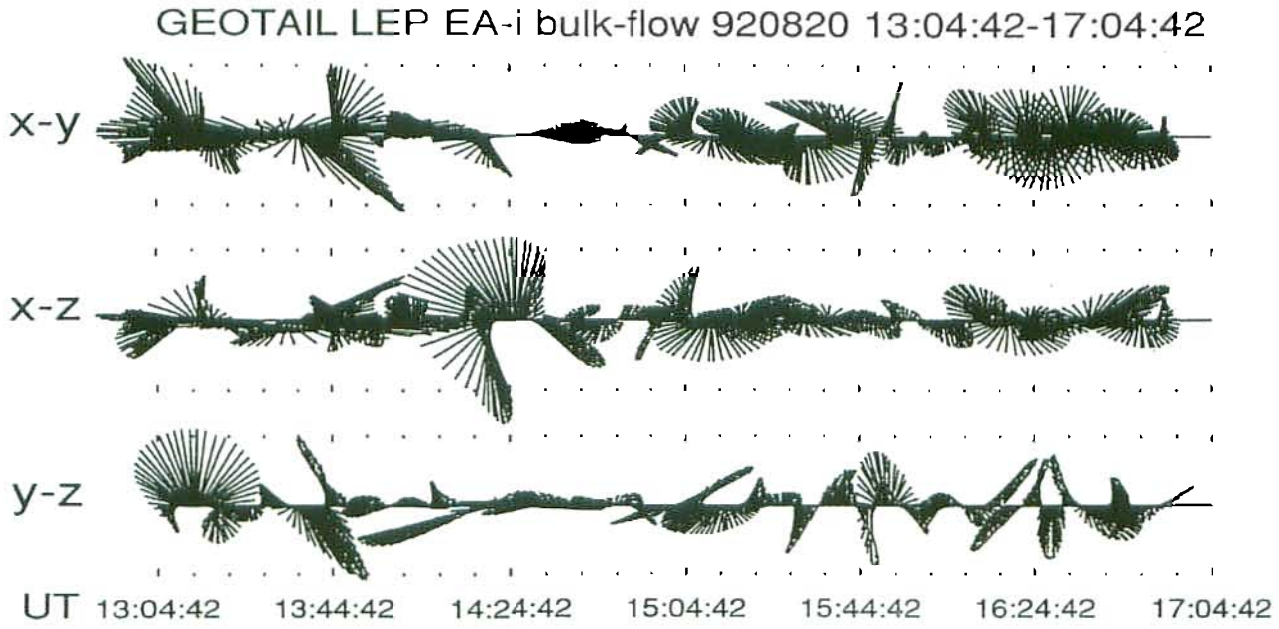

Fig. 13. Temporal variation of the fast varying component of the plasma bulk flow velocity projected on the *x-y*, *y-z* and *z-x* planes in the GSE coordinates.

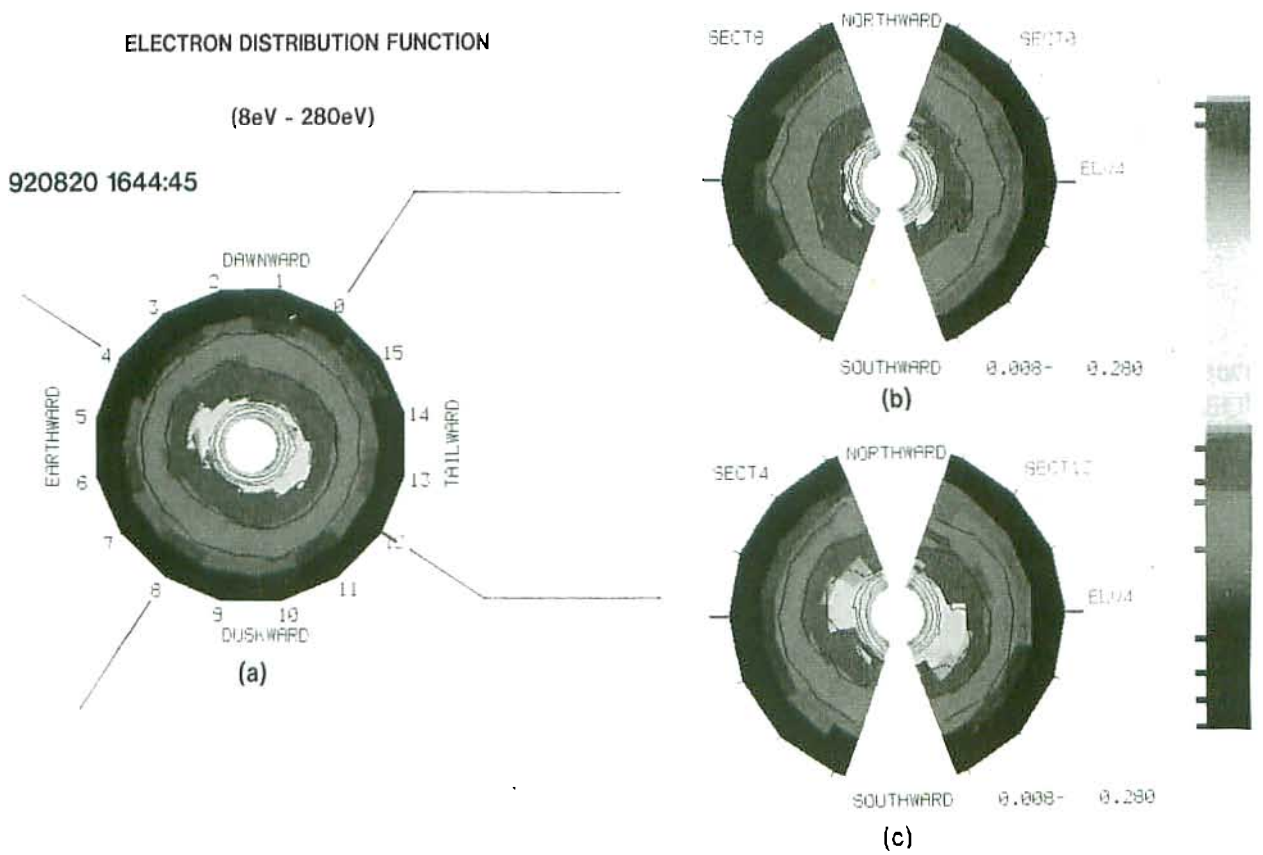

Fig. 14. Example of electron distribution functions in the three-dimensional phase space. Panel (a) shows the azimuthal distribution on the equatorial plane, while Panels (b) and (c) show the elevational distributions in two orthogonal azimuthal directions. The radial scale in each panel is linearly proportional to the electron velocity in the energy range below 280 eV.

private communication). Figure 12 shows comparison of the density, velocity and perpendicular temperature of ions obtained by the onboard moment calculation with those calculated from the three-dimensional distributions on the ground. The number of data points is four times larger in the onboard results than in the results of the ground calculation. It should be noted that the ground calculation is based on the background-subtracted data, while the background noise is not subtracted in the onboard calculation. None the less, both results generally agree very well, so that they are completely overlapped in most of the time. However, the difference is significant in the velocity data during the time interval of 1330–1340 in the high-speed region of low density. The background subtraction logics will also be incorporated in the onboard calculation in future.

In Fig. 12, one of the notable features is a highly dynamic variation of the plasma bulk flow direction in spite of the quiet geomagnetic condition. Similar variations have also been observed by the ISEE-1/2 satellites in the regions closer to the earth (e.g., Hones *et al.*, 1981) and by the ISEE-3 satellite in the distant tail (Sanderson *et al.*, 1984), but this is the first observation of the three-dimensional characteristics in the mid-tail region. A detailed description of this event is given in Saito *et al.* (1993). The dynamic spectrum of the variation of the bulk velocity magnitude (their Fig. 2) have revealed that the variation consists of two components with periods of ~8 minutes and ≥20 minutes, respectively. Figure 13 shows the temporal variation of the fast varying component, in which clear rotations can be seen in many periods of time, especially between 1606 UT and 1646 UT. The slowly varying component is directed roughly along the average direction of the magnetic field estimated from the electron pressure anisotropy assuming that the distribution is gyrotropic. An example of three-dimensional distributions of electrons is shown in Fig. 14, in which the magnetic field direction is estimated roughly as the direction of the elongated distribution;

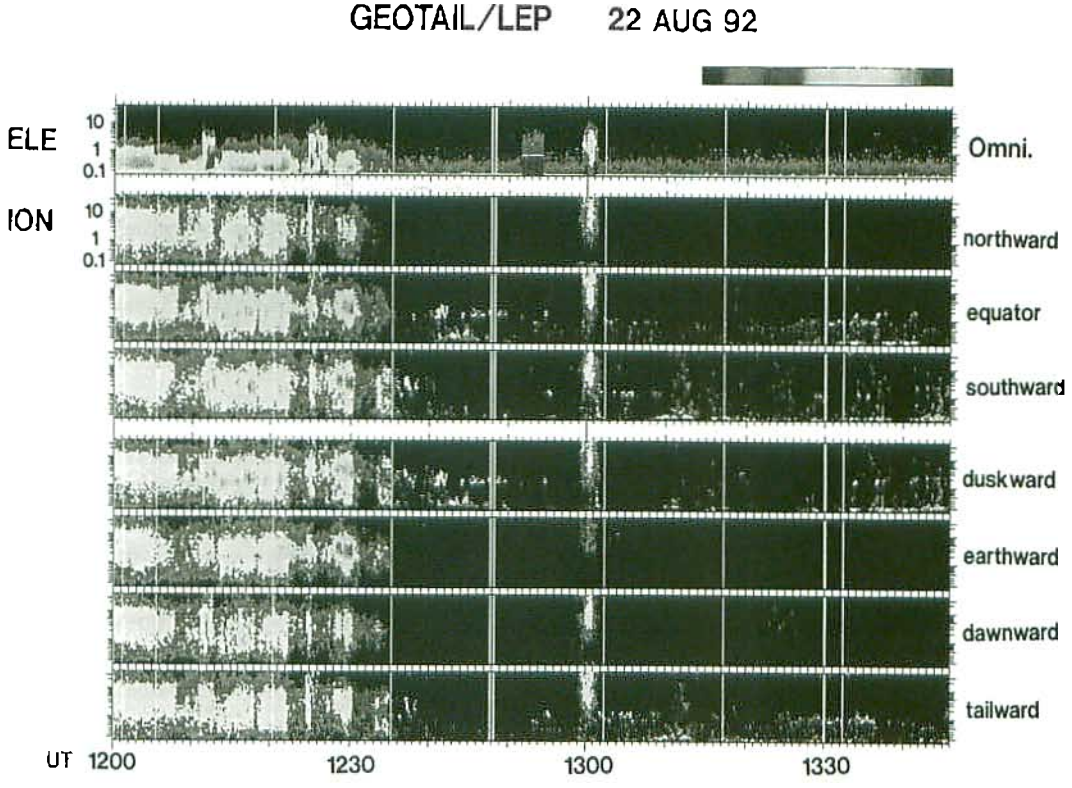

Fig. 15. Similar to Fig. 12, except that the data were obtained during the time interval of 1200 to 1346 UT on August 22, 1992. It should be noted that the electron energy during the time interval of 1251:46–1254:22 UT is not scaled by the ordinate, since the mode of electron energy scanning was changed to the B-mode in order to measure the detailed spectra in lower energies (see also Fig. 11).

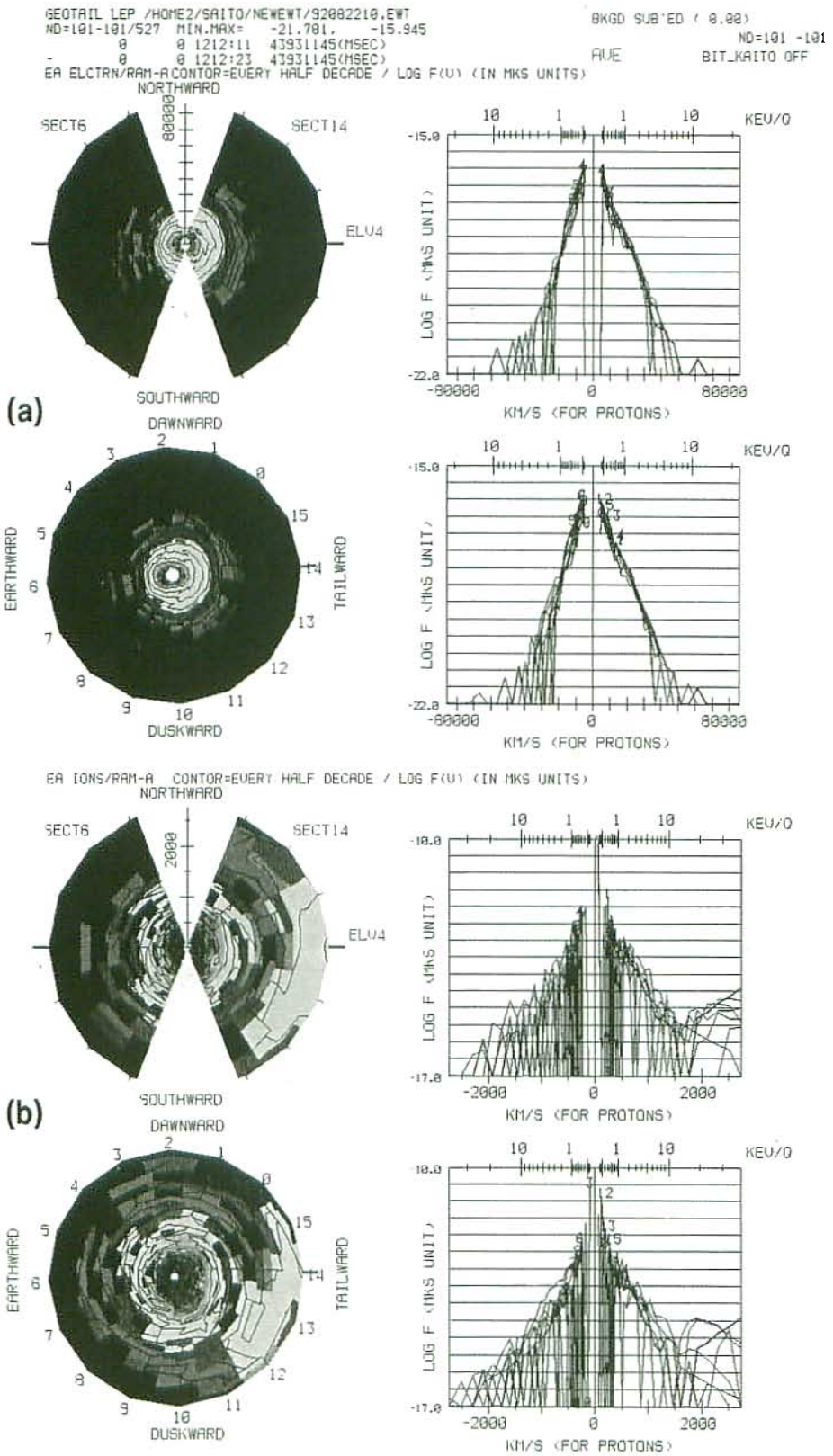

Fig. 16. Three-dimensional velocity distributions of (a) electrons (upper two panels) and (b) ions (lower two panels) observed at 1212:11–1212:23 UT during the first energetic particle event on August 22, 1992. The format of data display in each panel is similar to that of Fig. 11, but the phase space density in unit of s^3/m^6 on a logarithmic scale is coded by color in the left-hand panels and are shown by the ordinates in the right-hand panels.

in this case, $P_{\parallel} > P_{\perp}$.

Figure 15 shows the electron and ion data observed at $X_{GSM} \sim -42$ Re, $Y_{GSM} \sim 5$ Re and $Z_{GSM} \sim 2$ Re on August 22, 1992. The spacecraft was located in the plasma sheet from the beginning of the time period shown, 1200 UT, up to ~1235 UT. Hot plasma with keV-energy ions was observed continuously, though the energy density was variable. Electron data also exhibited similar features. After ~1235 UT, the hot plasma density decreased drastically, and the spacecraft remained in the lobe region until the end of the observation period. The geomagnetic conditions were quite active ($K_p = 5_-$) during the observation interval, and the ground magnetogram data in the 210° magnetic meridian indicated a Pi-2 onset at 1208 UT as a substorm signature (Yumoto, private communication). In Fig. 15 three bursty events of high-speed tailward plasma flows with duration of ~1 minute are evident around 1212 UT, 1225 UT and 1300 UT. Figure 16 shows an example of the three-dimensional velocity distributions of electrons and ions, which were observed in the first event when the spacecraft was in the plasma sheet. The ion distribution consists of two components, the lower-energy component representing the stationary plasma sheet proper and the higher-energy component flowing tailward with speed of ~2,000 km/s. The electron distribution also show an interesting feature that is counterstreaming in lower energies and isotropic in higher energies. More detailed descriptions of these events are given in Machida *et al.* (1994).

Another interesting feature in Fig. 15 is that in the lobe region after ~1235 UT, beam-like distributions at two discrete energies of ~100 eV/q and 1–2 keV/q are detected instead of the previously-observed hot component of the plasma sheet proper. The cold ion beams are generally flowing tailward and southward. They are most likely to be protons (lower-energy component) and singly charged oxygen ions (higher-energy component), which would be transported from the polar ionosphere of the dayside cusp/cleft region. The dynamics of these cold ion beams are discussed in more detail separately in Mukai *et al.* (1994a, 1994b).

4. Concluding Remarks

The initial observations have confirmed the high-quality performance of the LEP instrument having three-dimensional measurement capability with fine time resolution. The observed data have demonstrated a highly dynamic variability of the mid-tail plasma. However, part of the low-voltage electronics in LEP-E was latched up soon after the observation shown in Fig. 15, and thereafter the operation of the LEP instrument had become suspended. Fortunately, the latch-up was released by a special operation (instantaneous shutdown of the spacecraft power) in a lunar eclipse on September 1, 1993. The instrument performance has recovered, and the LEP experiment is producing again the key information for resolving the open questions summarized in the Introduction.

We thank all members of GEOTAIL project team in Japan as well as in the U.S.A for their extensive efforts to the success of GEOTAIL, especially K. T. Uesugi, the Project Manager of ISAS, and K. Sizemore, the Project Manager of NASA/Goddard Space Flight Center. Recovery of the LEP instrument due to the September-1 eclipse operation would not be made possible without the efforts of many people, in particular K. T. Uesugi, M. H. Acuna, K. Tsuruda, I. Nakatani, M. Hashimoto, H. Hayakawa, T. Yamamoto, M. Nakamura, the ISAS/GOOD (Group Of Orbit Design) team, and NEC corporation (especially, T. Orii, M. Kamimura, M. Kawaguchi, K. Takahashi, and T. Tohma). We also appreciate the GEOTAIL Principal Investigators for their encouragements. The electronic part and the sensor units in the LEP instrument were manufactured by Meisei Co. Ltd., and Mitaka-koki Co. Ltd., respectively. The microchannel plates were developed by Hamamatsu Photonics Co. Ltd.

REFERENCES

Ashour-Abdalla, M., J. P. Berchem, J. Büchner, and L. Zelenyi, Shaping of the magnetotail from the mantle: global and local structuring, *J. Geophys. Res.*, **98**, 5651–5676, 1993.

Baker, D. N., R. C. Anderson, and R. D. Zwickl, Average plasma and magnetic field variations in the distant magnetotail associated with near-earth substorm effects, *J. Geophys. Res.*, **92**, 71–81, 1987.

Baumjohann, W., The near-earth plasma sheet: an AMPTE/IRM perspective, *Space Sci. Rev.*, 1993 (in press).

Delcourt, D. C., J. A. Sauvaud, and T. E. Moore, Polar wind ion dynamics in the magnetotail, *J. Geophys. Res.*, **98**, 9155–9169, 1993.

Eastman, T. E., L. A. Frank, W. K. Peterson, and W. Lennartsson, The plasma sheet boundary layer, *J. Geophys. Res.*, **89**, 1553–1572, 1984.

Gosling, J. T., J. R. Asbridge, S. J. Bame, and W. C. Feldman, Effects of a long entrance aperture upon the azimuthal response of spherical section electrostatic analyzers, *Rev. Sci. instr.*, **49**, 1260–1268, 1978.

Hones, E. W., Jr., J. Birn, S. J. Bame, J. R. Asbridge, G. Paschmann, N. Sckopke, and G. Haerendel, Further determination of the characteristics of magnetospheric plasma vortices with Isee 1 and 2, *J. Geophys. Res.*, **86**, 814–820, 1981.

Hones, E. W., Jr., D. N. Baker, S. J. Bame, W. C. Feldman, J. T. Gosling, D. J. McComas, R. D. Zwickl, J. A. Slavin, E. J. Smith, and B. T. Tsurutani, Structure of the magnetotail at 220 R_E and its response to geomagnetic activity, *Geophys. Res. Lett.*, **11**, 5–7, 1984.

ISEE-3 Distant Geotail Results, *Geophys. Res. Lett.*, **11**, 1027–1105, 1984.

Lennartsson, W., R. D. Sharp, E. G. Shelley, R. G. Johnson, and H. Balsiger, Ion composition and energy distribution during 10 magnetic storms, *J. Geophys. Res.*, **86**, 4628–4638, 1981.

Lui, A. T. Y. (editor), *Magnetotail Physics*, The Johns Hopkins Univ. Press, 1987.

Lui, A. T. Y., Extended consideration of a synthesis model for magnetospheric substorms, *Geophys. Monogr.*, **64**, 43–60, 1991.

Lyons, L. R. and T. W. Speiser, Evidence for current sheet acceleration in the geomagnetic tail, *J. Geophys. Res.*, **87**, 2276–2286, 1982.

Machida, S., T. Mukai, Y. Saito, T. Obara, A. Nishida, M. Hirahara, T. Terasawa, and K. Maezawa, Plasma distribution functions in the Earth magnetotail (X_{GSE} ~ –42 Re) at the time of the magnetospheric substorm: GEOTAIL/LEP observation, *Geophys. Res. Lett.*, 1994 (in press).

Mukai, T., W. Miyake, T. Terasawa, and K. Hirao, Observations of solar wind ions by the interplanetary spacecraft Suisei (PLANET-A), *J. Geomag. Geoelectr.*, **39**, 377–395, 1987.

Mukai, T., M. Hirahara, S. Machida, Y. Saito, T. Terasawa, and A. Nishida, GEOTAIL observation of cold ion streams in the medium distance magnetotail lobe in the course of a substorm, *Geophys. Res. Lett.*, 1994a (in press).

Mukai, T., M. Hirahara, S. Machida, Y. Saito, T. Terasawa, and A. Nishida, Initial observations of the medium distance magnetotail plasma by GEOTAIL: cold ion beams, *Geophys. Monogr.*, 1994b (in press).

Nakamura, M., G. Paschmann, W. Baumjohann, and N. Sckopke, Ion distributions and flows in and near the plasma sheet boundary layer, *J. Geophys. Res.*, **97**, 1449–1460, 1992.

Peterson, W. K., R. D. Sharp, E. G. Shelley, R. G. Johnson, and H. Balsiger, Energetic ion composition of the plasma sheet, *J. Geophys. Res.*, **86**, 761–767, 1981.

Saito, Y., T. Mukai, S. Machida, M. Hirahara, A. Nishida, and T. Terasawa, Rapid variations of the plasma bulk flow direction observed in the plasma sheet at X_{GSE} ~ –60 Re, *Geophys. Res. Lett.*, 1993 (in press).

Sanderson, T. R., P. W. Daly, K. P. Wenzel, E. W. Hones, Jr., and S. J. Bame, Energetic ion observations of a large scale vortex in the distant tail, *Geophys. Res. Lett.*, **11**, 1094–1097, 1984.

Sharp, R. D., W. Lennartsson, W. K. Peterson, and E. G. Shelley, The origin of the plasma in the distant plasma sheet, *J. Geophys. Res.*, **87**, 10420–10424, 1982.

Speiser, T. W., Particle trajectories in model current sheets, 1. analytic solution, *J. Geophys. Res.*, **70**, 4219–4226, 1965.

Takahashi, K. and E. W. Hones, Jr., ISEE 1 and 2 observations of ion distributions at the plasma sheet-tail lobe boundary, *J. Geophys. Res.*, **93**, 8558–8582, 1988.

Correction:

The content of Table 5 is changed as follows.

Table 5 Basic parameters of the instrument performance for the SW sensor.

SW				
CHANNEL (DIRECTION)	$\Delta\alpha$ (FWHM)	$\Delta\theta$ (FWHM)	$\Delta\delta$ (FWHM)	g-factor ($cm^2 \cdot str \cdot eV/eV$)
CH1 (−25.2°)	2.5°	8.0°	3.7 %	7.84×10^{-6}
CH2 (−17.2°)	2.5°	8.9°	3.9 %	9.97×10^{-6}
CH3 (−8.6°)	2.5°	8.3°	3.9 %	1.00×10^{-5}
CH4 (0.0°)	2.5°	8.3°	4.0 %	9.81×10^{-6}
CH5 (8.7°)	2.6°	8.4°	4.2 %	1.05×10^{-5}
CH6 (17.3°)	2.7°	8.6°	4.5 %	1.06×10^{-5}
CH7 (26.0°)	2.8°	9.0°	4.4 %	1.07×10^{-5}